Supplementary Materials for Vanadium in Silicon Carbide: Telecom-ready spin centres with long relaxation lifetimes and hyperfine-resolved optical transitions

Thomas Astner
Institute for Quantum Optics and Quantum Information (IQOQI) Vienna, Austrian Academy of Sciences, Boltzmanngasse 3, 1090 Vienna, Austria and Vienna Center for Quantum Science and Technology, Universität Wien, Boltzmanngasse 5, 1090 Vienna, Austria

Philipp Koller
Institute for Quantum Optics and Quantum Information (IQOQI) Vienna, Austrian Academy of Sciences, Boltzmanngasse 3, 1090 Vienna, Austria Vienna Center for Quantum Science and Technology, Universität Wien, Boltzmanngasse 5, 1090 Vienna, Austria and University of Vienna, Faculty of Physics & Vienna Doctoral School in Physics, Boltzmanngasse 5, A-1090 Vienna, Austria

Carmem M. Gilardoni and Joop Hendriks
Zernike Institute for Advanced Materials, University of Groningen, NL-9747AG Groningen, The Netherlands

Nguyen Tien Son, Ivan Gueorguiev Ivanov, and Jawad Ul Hassan
Department of Physics, Chemistry and Biology, Linköping University, SE-581 83 Linköping, Sweden

Caspar H. van der Wal
Zernike Institute for Advanced Materials, University of Groningen, NL-9747AG Groningen, The Netherlands

Michael Trupke
Institute for Quantum Optics and Quantum Information (IQOQI) Vienna, Austrian Academy of Sciences, Boltzmanngasse 3, 1090 Vienna, Austria and Vienna Center for Quantum Science and Technology, Universität Wien, Boltzmanngasse 5, 1090 Vienna, Austria

(Dated: April 8, 2024)

This document presents supplementary information to the main text, such as an overview of the experimental apparatus, methods and additional measurement results.

I. EXPERIMENTAL METHODS

A. Samples

All measurements in the main text were carried out with commercially available semi-insulating SiC material, purchased from the company II-VI. We cut 5 mm x 5 mm chips from wafers with a diamater of 100 mm and an average thickness of 496 µm. In our experiments we use the polytypes 4H- and 6H-SiC with a vanadium concentration of $1 \times 10^{17}\,\mathrm{cm}^{-3}$. Other impurities like boron and nitrogen have a concentration of $1 \times 10^{16}\,\mathrm{cm}^{-3}$ and aluminium below $1 \times 10^{16}\,\mathrm{cm}^{-3}$.

B. Setup and Optical Measurements - Vienna

In all optical measurements we interface the vanadium defects by coupling light to the centers with a standard FC/PC fiber connector at the end of a SMF-28 fiber (NA= 0.14), by mounting the connector on a spring loaded

copper plate which ensures planar contact of the connector tip on the SiC chip surface. This simple and robust approach trades convenience for collection efficiency, which was, however, not a limitation in our measurements given the strong luminescence signal of the ensembles studied herein. The direction of the optical excitation is parallel to the wafer c-axis. The emitted photoluminescence is collected through the same fiber and detected with a superconducting single photon detector (Single Quantum). The signal and timings are detected with an 100 MHz data acquisition card (National Instruments).

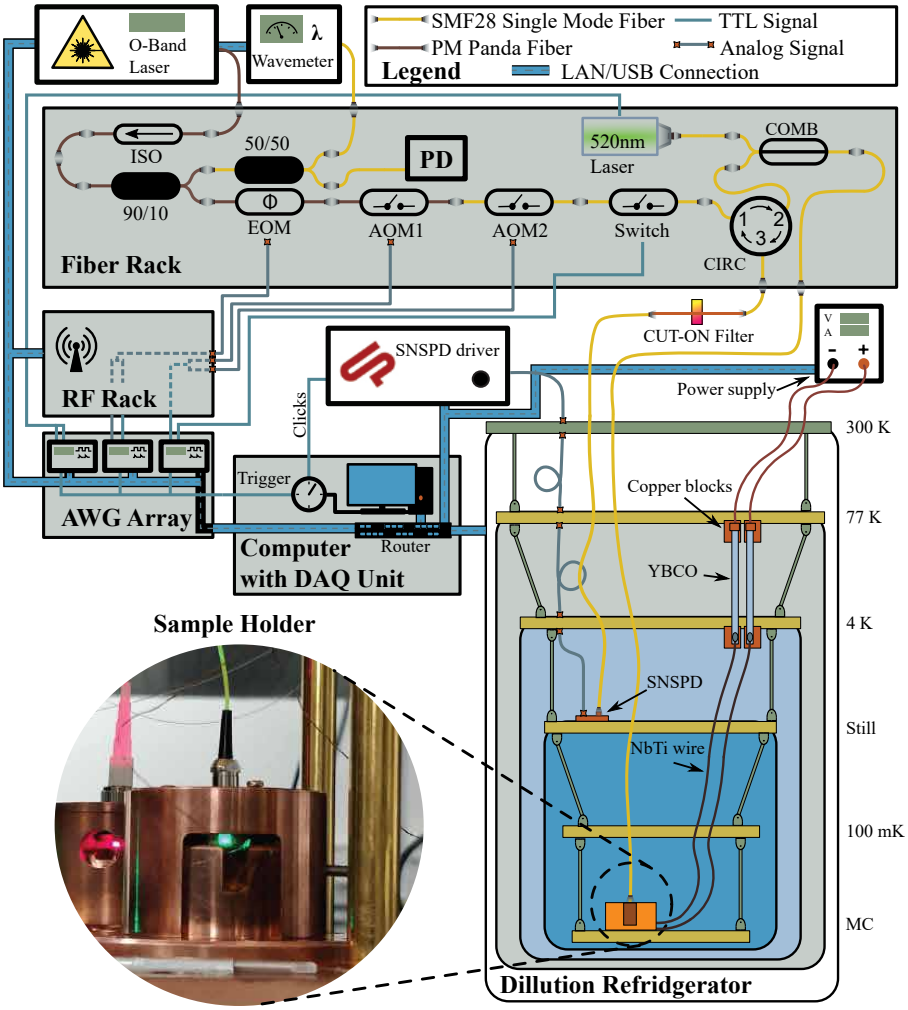

FIG. 1. **Setup:** This illustration gives an overview of the used setup. Key elements are the tunable laser, EXFO T100S-HP (1260 nm to 1360 nm, $P_{max} = 13$ dBm) and the superconducting nanowire single photon detector (Single Quantum). The sample is enclosed in a copper sample holder and mounted at the lowest stage of a dilution refrigerator (Oxford Instruments). In the sample holder a superconducting solenoid with 4000 turns is mounted and is used to generate magnetic fields of 245 mT A^{-1} at the sample. Light is coupled to the sample with a standard FC/PC fiber connector that is spring loaded and provides direct contact with the sample.

The crystal with the fiber on top is enclosed in a copper sample holder with a superconducting solenoid below which is used to generate a magnetic field parallel to the wafer c-axis. The coil current to magnetic field conversion is found to be 245 mT A^{-1} from the known g-factors of the transitions, in agreement with a numerical simulation. Mounting the sample holder on the lowest stage of a dilution refrigerator enables us to carry out measurements at temperatures between 30 mK and 2 K.

We use a tuneable telecom O-band laser as source for resonant optical excitation. Part of the output laser light is monitored with a wavemeter (HighFinesse WS6-200 IR-I) and a photodiode. A fiber electro-optical modulator (Optilab PM-1310-5) is used to create the sidebands for two-photon spectroscopy measurements. Pulses are created

with two fiber acousto-optical modulators in series, with a risetime of less than 20 ns and an off-state suppression of 90 dB. A fiber circulator and an optical longpass filter (1300 nm or 1350 nm) are used to separate the reflected excitation laser light from phonon sideband emission. With a combiner, green laser light is added to the optical excitation path. Fig. 1 shows an illustration of the setup with its major components.

II. PLE SPECTROSCOPY

To identify the optical transitions of the defects, resonant photoluminescence emission (PLE) spectroscopy was performed by sweeping the laser over the zero phonon line, while collecting the photons emitted in the phonon sideband. We investigated the α site in 4H-SiC (4H-α), the β site in 4H-SiC (4H-β) and the α site in 6H-SiC (6H-α). All spectra are recorded at a temperature of around 100 mK.

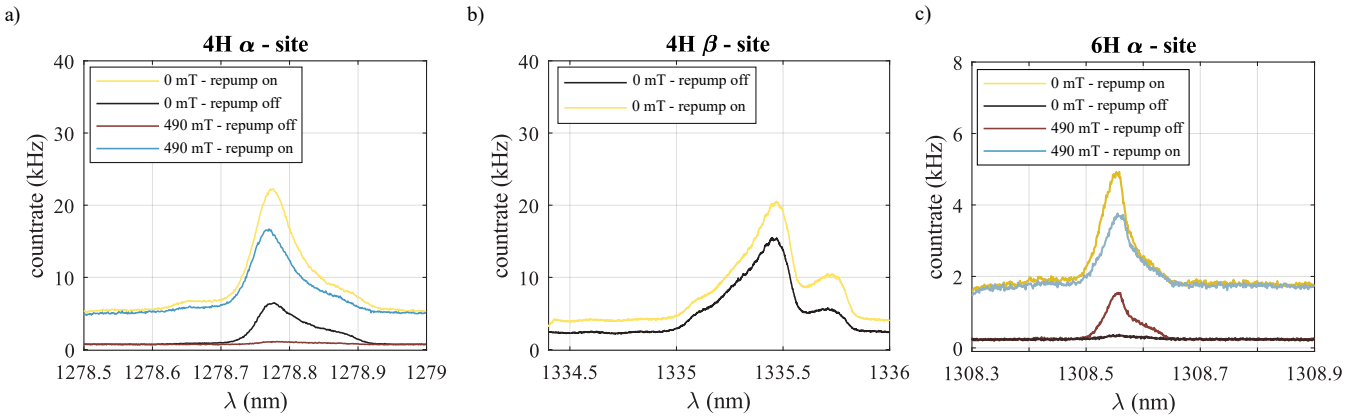

FIG. 2. **PLE comparison in 4H and 6H.** a) Low temperature spectrum of the 4H-α defect GS1-ES1 transition. The resonance signal is recorded at zero magnetic field and at 490 mT, each with and without above bandgap green laser illumination (repump on/off). b) PLE signal of the GS1-ES1 and GS2-ES1 transition of the 4H-β site with and without repump green laser. c) PLE spectroscopy of the 6H-α site GS1-ES1 transition. The spectrum is recorded at 100 mK with/without magnetic field and repump laser on/off.

A. Resonances in 4H- and 6H-SiC

The results of PLE measurements of GS1 to ES1 transition in 4H-α and 6H-α are shown Fig. 2 a) and c). Adding a magnetic field leads to a reduction of fluorescence, due to the optical splitting of the transitions. By adding continuous wave green laser light the fluorescence at zero magnetic field is boosted, and the feature can also be observed with magnetic field. The offset seen in the plot is attributed to leakage and emission from all possible defects within the crystal, as they are driven by the green laser light. For neither of the defects any transitions involving the GS2 or ES2 is observed.

The results of the PLE measurement of the 4H-β defect can be seen in Fig. 2 b). Here the GS1-ES1 and GS2-ES1 transitions were observed. Adding green illumination increases the signal from the GS2-ES1 transition.

B. Sample Comparison

We compare the commercially availible 4H-SiC material to a custom-grown sample with a 24 µm thick epitaxial layer with a vanadium concentration of $1 \times 10^{15}\,\mathrm{cm}^{-3}$. Fig. 3 presents the 4H-α PLE spectra acquired from the two samples. The spectrum of the epitaxial sample was measured with above-bandgap re-pump illumination to populate

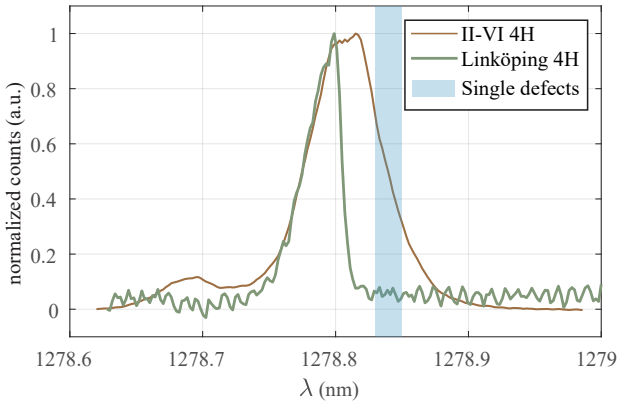

FIG. 3. **Line shapes of the 4H-α GS1-ES1 transition.** The figure shows a comparison between a highly doped commercial grade wafer and an epitaxially grown layer ("Linköping 4H"). The lineshape is visibly reduced in the epitaxial sample (31 pm FWHM), compared to the spectrum of the commercial wafer (65 pm FWHM). Both traces are peak normalized. The shaded area indicates the wavelength range of single defects [1, 2].

the neutral charge state. The wavelength of the laser is monitored with a wavemeter to obtain absolute wavelength precision to better than ±20 pm. We note that the emission wavelength of single defects is 1278.85 nm, lying outside the distribution of the epitaxial layer and on the slope of the commercial sample emission [1]. The origin of this discrepancy calls for further investigation.

III. CHARGE STATE SWITCHING

A. Candidate mechanisms for charge state dynamics

The V^{4+} neutral state is the only charge state of vanadium in 4H-SiC that features luminescence in the telecom O-band. The other known bandgap charge states are V^{3+} and V^{5+}[3, 4]. In our experiments, the V^{4+} charge state is populated by illumination with a 520 nm green laser pulse. Prolonged, high-power illumination of the GS-ES transition results in a reduction of the observed fluorescence signal for resonant vanadium defects due to charge state conversion [1, 2, 5], which we tentatively ascribe to two mechanisms:

- Conversion from V^{4+} to the dark V^{5+} state by a two-photon process, where the electron in the optically excited state is further excited to the conduction band by the absorption of a second photon; and
- Conversion from V^{4+} (bright) to V^{3+} (dark), by the resonant laser promoting electrons from the C vacancy donor into the conduction band. Subsequently, these electrons are preferentially captured by V^{4+} when it is in the optically excited state, leading to the observed bleaching around the laser excitation frequency. The hypothesized mechanism is similar to what has been proposed for the NV center in diamond. For vanadium, however, the captured electrons must originate from inter-bandgap defects, rather than from the valence band [6].

The charge transition levels pertaining to these state conversion mechanisms are depicted in Fig. 4.

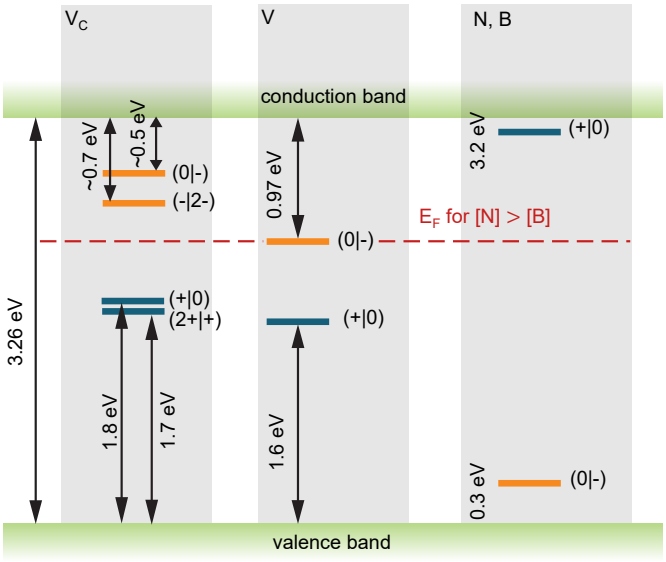

FIG. 4. **Charge transition levels in 4H-SiC.** The main charge transition levels of vanadium in SiC are presented, together with the main dopants nitrogen (N) and boron (B). For example, (+/0) denotes the transition of the positively charged vanadium (V^{5+}) to the neutral (V^{4+}). Additionally, the Fermi level for the samples used in this work is shown.

B. Holeburning measurements

With a high power IR laser light it is possible to engineer the line shape of the PLE spectra of the defects in the 4H-SiC crystal. To do so, we stabilize the laser with a wavemeter and illuminate the GS1-ES1 transition at 100 mK. Pumping for 60 seconds results in ionization of the charges in this spectral range resonant with the laser beam. The PLE signal strength at this position is significantly reduced. Also, no spontaneous recovery of the charges was observed and the charge holes were stable for at least two hours after creation (see Fig. 6 a)). Using off resonant excitation (520 nm) the initial charge state can be reinstated.

This bleaching was more efficient in 4H-α (Fig. 5) than in 4H-β (Fig. 5). Interestingly, burning a spectral hole in the peak of the β resonance, resulted in copies of the hole shifted by the GS1-GS2 splitting, as shown in Fig. 6. This indicates that some defects' GS1-ES1 and GS2-ES1 transitions were resonant with the laser frequency during the burning. In contrast to this observation, we could not see any spectral bleaching in the 6H-α defect.

IV. TWO LASER SPECTROSCOPY

To gain information on the hyperfine structure of the defect, we perform two laser spectroscopy, by generating sidebands with an electro-optic modulator (EOM). Two different schemes were utilized and are illustrated in Fig. 7. Applying a RF signal to the EOM creates two sidebands with a relative shift to the center laser wavelength. The sidebands are blue and red detuned to the carrier by the driving frequency of the EOM. Varying the driving frequency of the EOM results in sweeping sidebands. In the scheme depicted in Fig. 7 a), the carrier is resonant with the defects GS1 - ES1 transition. Both sidebands are within the spectral feature, which results in several possible transitions between the carrier and the sidebands, but also sideband to sideband transitions are possible. This creates copies of the observed features at half the feature frequency. In order to eliminate these copies, we have extended the scheme with an additional sideband, generated by a second RF tone. This scheme is illustrated in Fig. 7 panel b). The carrier is detuned from the peak of the spectral feature. Two fixed sidebands at 4.5 GHz and a second pair of variable sidebands which are used to sweep through the feature are applied. All blue-detuned sidebands and the carrier are set far from the peak of the PLE feature and have a minor contribution to the overall spectroscopy signal. Only the two red-detuned sidebands are within the ensemble linewidth and will lead to an observable two-photon PLE signal.

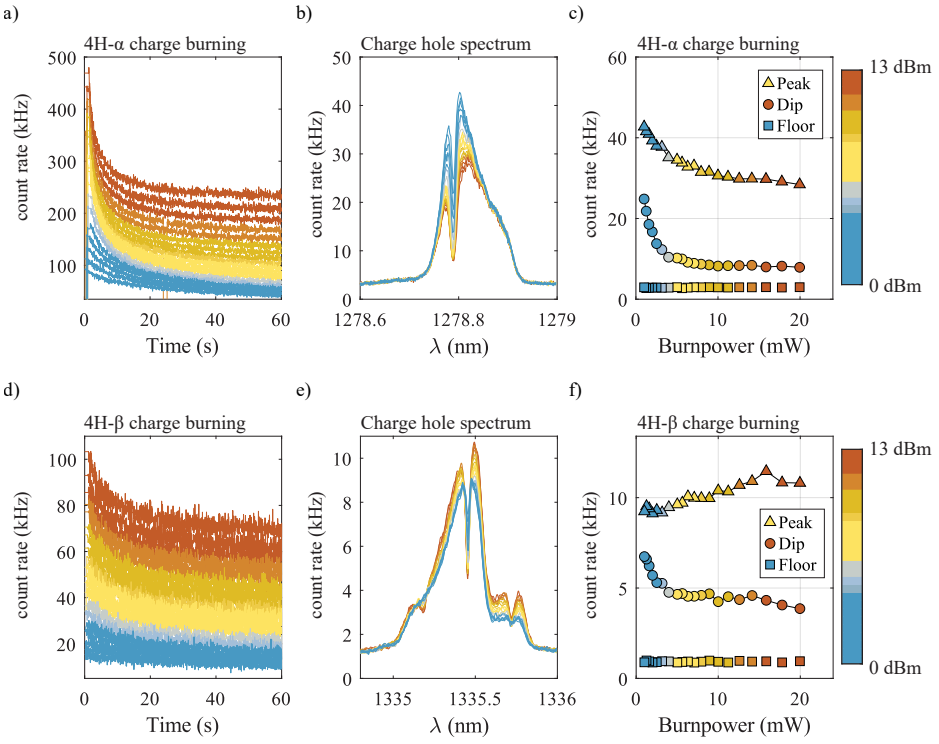

FIG. 5. **Charge state switching in 4H.** The applied laser power corresponds to the color coding: from blue at 0 dBm to red at 13 dBm laser output power. Panels a) to c) display measurements on 4H-α and d) to f) on 4H-β. a), d) Bleaching of the recorded fluorescence during the 60 s burn pulse. b), e) PLE of the defect after the burning using a sweep with short integration time (200 ms per point) at low power (-3 dBm) to avoid ionization. c), f) The recorded maximum (peak), minimum (floor), and the value of counts recorded at the wavelength of the charge hole (dip).

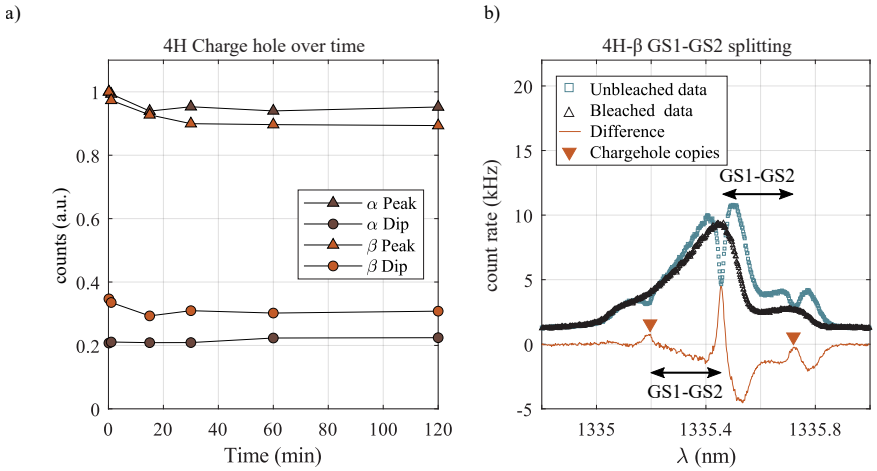

FIG. 6. **Charge switching in 4H.** a) Dip and peaks of the charge switched PLE spectra for the 4H-α and β defects measured with varied delays from 10 s to 2 hours. b) Comparison of the unbleached to the bleached PLE spectrum of 4H-β at the highest burn power. A clear increase of the GS2 population can be observed. The frequency difference between the hole and the copies is indicated by a double arrow and shows the relative splitting between GS1 and GS2.

These measurements were performed at 0.1 K. To counteract frequency dependent fluctuation and time dependent drifts during the measurement, the recorded data was post-processed. From each data point in the scan a moving mean was subtracted in the y-direction so frequency dependent errors were counteracted and in the x direction to eliminate time dependent external effects (e.g. lights in the laboratory or variations in the collection efficiency). We use a Wiener filter on the data set to reduce measurement noise and improve the visibility of the features.

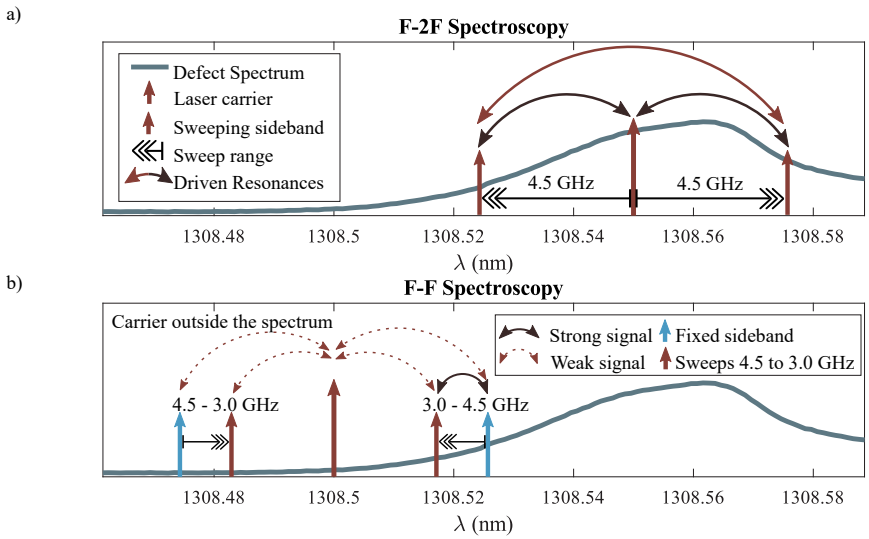

FIG. 7. **Two-laser spectroscopy scheme.** a) Schematic showing the F-2F two laser spectroscopy scheme on an example 6H-α resonance. The carrier is positioned at the center of the resonance and the two sidebands sweep the full range of 4.5 GHz symmetrically. Transitions are driven not only between the carrier and the sidebands, but also between the two sidebands, leading to copies of each feature in the spectrum. b) Schematic of the F-F spectroscopy method, showing the positions of the carrier and sidebands as they were used in the experiment. The carrier is outside the resonance to contribute less to the collected fluorescence, one sideband is fixed at 4.5 GHz and a second sideband sweeps a reduced range from 4.5 GHz to 3.0 GHz. Which transition is driven depends on the difference between the two sidebands.

Two laser PLE-spectroscopy data was fitted to equation 1 to determine the hyperfine parameters. The magnetic field calibration was performed using the known g-factor and hyperfine parameters for 4H-α [1, 3]. These parameters were not determined independently in the measurements, but agree with the observed features. The g-factor of the excited state was then extracted from the gradient of the spin-conserving transitions at high field (Fig. 3b). The hyperfine terms of the excited state were found using the zero-field features of the V-type transitions (Fig. 2c) and one of the features resulting from transitions involving different nuclear spin states, with zero first-order magnetic field sensitivity near 19 mT and a frequency difference of 0.15 GHz (Fig. 3e).

A. Two laser spectroscopy of 6H-α

For the 6H-α defect a two laser spectroscopy experiment was performed in the same fashion as for the 4H-α defect (presented in the main text of the manuscript). The result of this measurement can be seen in Fig. 8 and is very similar to its counterpart in 4H. Here also V-type and Λ-type resonances, as well as V* and Λ*, have been observed. At high fields, Π-type transitions start to dominate the spectrum.

B. Two laser spectroscopy of 4H-β

Due to the large linewidth of the 4H-β optical resonance, it was not possible to perform F-F spectroscopy but instead only one set of sidebands was applied. The results of this measurement can be seen in Fig. 9.

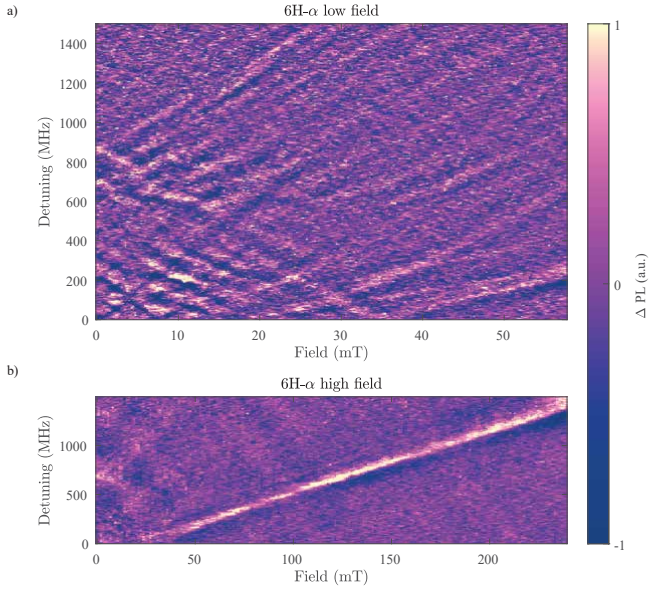

FIG. 8. Two laser spectroscopy scans using the F-F method, with two pairs of sidebands, one fixed and one sweeping, of the 6H-α site GS1-ES1 transition. The measurements was taken at around 100 mK, raw data was subtracted by a running mean in the x and y direction and noise was removed using a Wiener filter. a) Low field scan with high resolution of 1 MHz and 0.245 mT. Many bright and dark features can be seen as well as distinct crossing points of individual lines, even though less clear than in the 4H alpha site. b) High field scan with a resolution of 5 MHz and 1.2 mT.

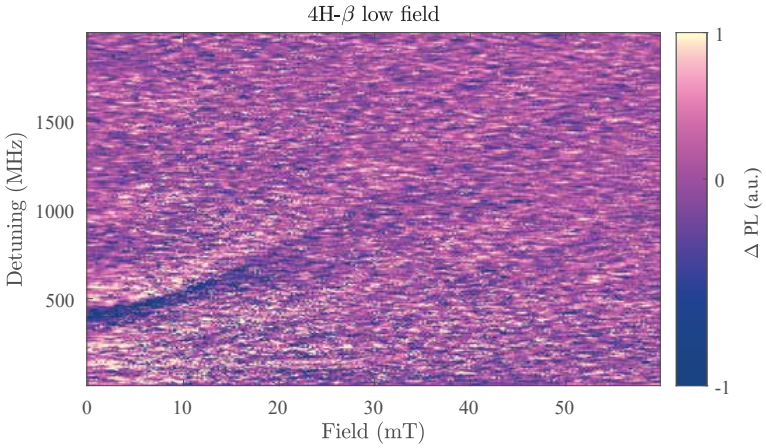

FIG. 9. Two laser spectroscopy scan using the F-2F method, with only one pair of sidebands, of the 4H-β site GS1-ES1 transition. Dark areas were observed but the signal was not sufficient to clearly resolve the level structure. The measurement was taken at around 100 mK, raw data was subtracted by a running mean in the x and y direction and signal was smoothed using a Wiener filter.

V. SPIN LATTICE RELAXATION - T_1

For the hole burning recovery sequence we pulse the laser output with two fast acousto-optic modulators (AOMs) with a rise time of 20 ns. The used scheme is illustrated in Fig. 10, showing the timing sequence, how population is driven to different states and the recorded signal. This sequence is repeated for different delay times τ and compared to the initial pulse. We integrate the measured counts in the time window of 10 µs and compare it to the initial pulse to determine the fractional population recovery. By tracking the fraction of recovered population as function of the delay time τ we are able to extract the relaxation rates by fitting an double exponential function in the form: $y = A(1 - e^{-\Gamma_0 \tau}) + B(1 - e^{-\Gamma_0 \tau}) + C$, to the recovery data, with the constraint: $A + B = 1 - C$, and all coefficients positive.

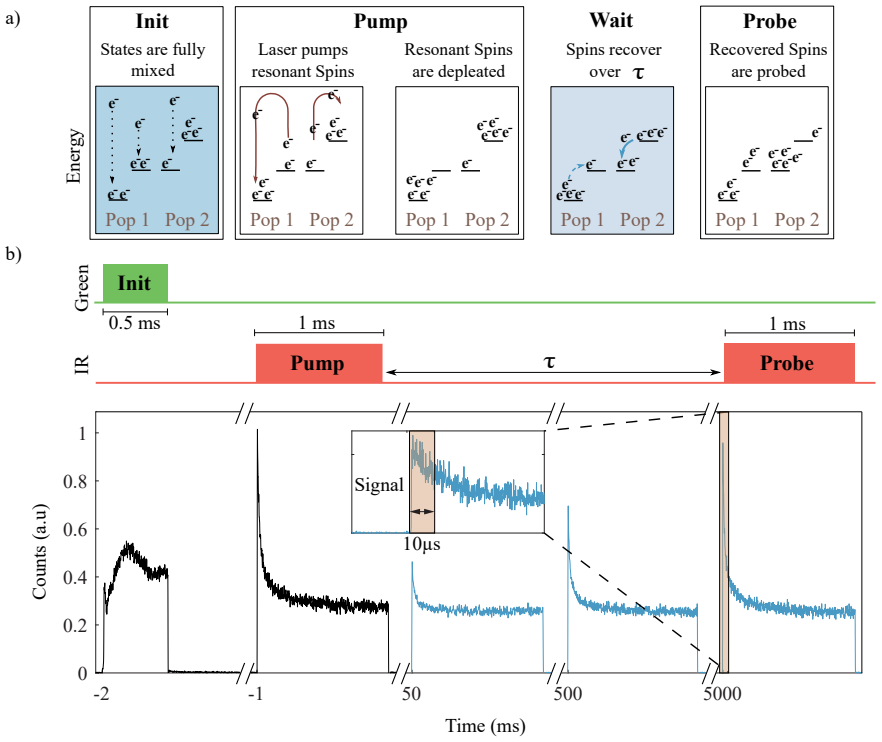

FIG. 10. **Hole burning recovery sequence and transient detection.** a) Illustration of the state population dynamics during the experimental sequence. b) The ensemble is first initialized by a green laser pulse that mixes the population. Next, a second laser pulse drives population into the other, off resonant, spin state. During a variable delay time τ, a fraction of the population relaxes back to thermal equilibrium. The second pulse is used to probe the population recovery of the initial state, allowing to determine the spin lattice relaxation time. The bottom panel of the figure is an example which shows the recorded normalized fluorescence signal for three different wait times taken at 1.1 K for the 6H-α site. The signal is integrated over a 10 µs time window, which is presented in the pulse (shaded area).

A. Pump-probe experiment with transient detection in 4H-β

We measured a pump probe recovery experiment on 4H-β at 100 mK. In Fig. 11 a full data set is presented which shows how the population recovers. The data is best fitted with a single exponential function, with a resulting relaxation constant of $T_1 \approx 100\,\mu s$.

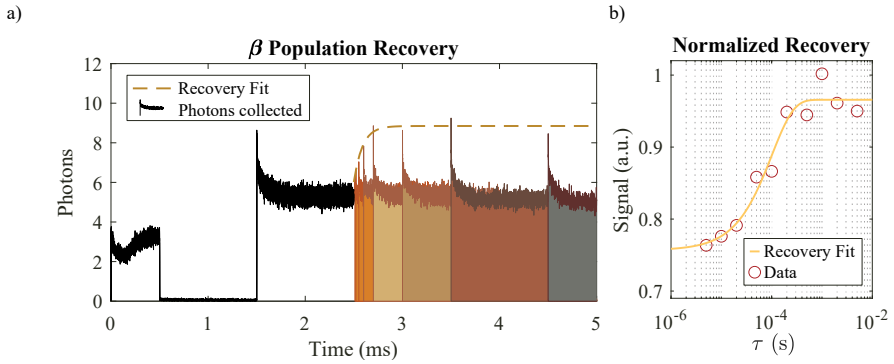

FIG. 11. **Population recovery.** a) Recorded fluorescence of the transient detection scheme for the 4H-β site for different delay times τ. Each sequence starts with a green initialization pulse and is followed by a pump pulse (non shaded area). After a variable delay time τ a readout pulse is used to determine the fraction of the recovered population. The measurement was recorded with a 10 ns resolution. To improve visibility, a 1 µs moving average of the data is shown. b) Resulting recovery signal and an exponential fit giving a spin lifetime $T1 \approx 100\,\mu s$.

B. Population recovery in 6H

In Fig. 12 the spin lattice relaxation recovery data for the 6H-α defect can be seen. The data was fitted with a double exponential, however, it was not possible to identify a characteristic fast decay constant. For this reason, the 1/e value was used to determine the spin relaxation rate.

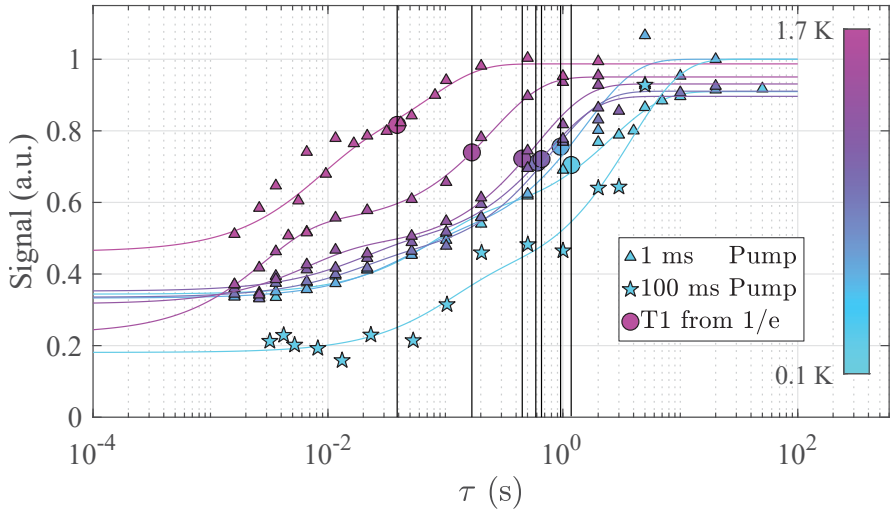

FIG. 12. Recorded fluorescence recovery signal of the α defect in 6H SiC. The data points measured with 1 ms initialization are displayed as triangles and the points measured with 100 ms initialization are displayed as stars. The recovery shows non exponential behaviour in both cases. Bi-exponential fits are shown as solid lines.

C. Measuring T_1 above 1.8 K

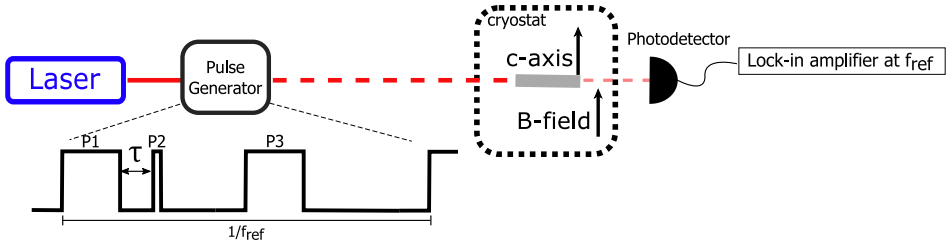

FIG. 13. Setup used for measuring T_1 at temperatures above 1.8 K. We use an absorption setup with continuous detection, where the measurement integration time required for good signal-to-noise ratio is significantly reduced by modulating the pulse sequence periodically and using a lock-in amplifier to extract the periodic signal detected by an InGaAs photodetector.

In the range between 1.8 K and 2.5 K, we used a different setup and measurement method to determine T_1, but we maintained the same optical pulse sequence with transient detection for extracting T_1. At these temperatures, the reduced spin relaxation time leads to a reduction in spin depletion and this results in low contrast for PLE detection of the spin relaxation behavior. For this reason, PLE-detection of the spin relaxation behavior in this regime requires collecting a large number of photons to obtain signals above the noise level. In our setup, this prohibitively increases the required averaging times. In order to circumvent this issue, we measure the transmission signal of a laser pulse sequence after passing through the sample instead. The signal is detected by a photodetector, whose output is fed to a lock-in amplifier which records the component of the signal at frequency f_{ref}. Section V F presents a derivation of how this lock-in detection is compatible with our pulse sequence. The rather high vanadium density (10^{17} cm^{-3}) and long

optical path (5 mm) combined provided a sample optically-thick enough for detecting changes in the hyperfine-sublevel populations via directly measuring optical absorption.

A schematic of the pulse sequence and the setup are shown in Fig. 13. We use a laser that is resonant with the α-line associated with V defects in a 4H-SiC sample, at 1278.72 nm. For the ensemble addressed, this wavelength provides the strongest laser absorption. The laser is continuously frequency stabilized to within 1 MHz of the set frequency. We generate a pulse train by using a combination of a phase-modulating EOM and a scanning Fabry-Perot interferometer (see also Ref. [7]). The EOM generates sidebands 1 GHz away from the carrier frequency, and it can be switched on/off in approximately 20 ns. The Fabry-Perot etalon is locked to one of the sidebands, and only transmits when the EOM is on. We create a pulse train consisting of three optical pulses linearly polarized perpendicular to the crystal c-axis. The first laser pulse P1 brings all defects at or near resonance with the laser from thermal equilibrium into a spin-polarized state. We underline that this mechanism does not necessarily result in an overall polarization of the probed ensemble. We used for pulse P1 (and P3) a duration of 1 ms, and when detecting these pulses after their propagation through the sample, we observed on their onsets transients due to this optical pumping (the transmitted block pulse has a rounded shoulder since absorption is moderately enhanced while the optical pumping towards its steady state dynamics is still in progress). At the optical powers we used these transients had a duration of about 200 μs. After a variable delay τ, we probe whether there is any re-population (due to spin relaxation) of a spin level that was pumped by P1. We do this with a short probe pulse P2 of 30 μs duration. This pulse is followed by a dark time that we set to at least five times longer than the measured T_1 time, during which the system can relax back to its thermal equilibrium spin distribution. Finally, we apply another pulse, P3, that is identical to the first pulse P1. This pulse P3 is the final optical pulse in the pulse train, and it is spaced at exactly half of the lock-in amplifier reference period T_{ref}. In this way, the signals from transmitted P1 and P3 cancel each other in the lock-in detection, and the remaining signal measured by the lock-in represents the integrated value of the detected transmission from pulse P2 (for details see Section V F). At a much slower timescale, we increase the delay between P1 and P2 (the delay τ). We thus obtain how the amplitude of the transmitted pulse P2 depends on the delay τ, which represents the τ-dependence of how much the spin populations in the ground state have restored to thermal equilibrium.

For these measurements, we use a wide spot size (approximately 100 μm in diameter) and, at most, 100 μW laser power at the sample. In these conditions, we do not observe significant bleaching of the defects due to charge state switching. Nonetheless, to counteract any residual bleaching, we apply a blue laser onto the sample for 2 s before collecting data at each delay τ. Magnetic fields are applied along the crystal c-axis.

D. Time-dependent transmission signal above 1.8 K

Figure 14 a) shows the time-dependent transmission signal measured using the lock-in amplifier as a function of the delay τ between pump and probe pulses (P1 and P2 in Fig. 13) for sample temperatures between 1.8 and 2.4 K. Traces were normalized respectively to each other and offset vertically for clarity. Black traces are fits to a biexponential decaying function ($y = Ae^{-\Gamma_0\tau} + Be^{-\Gamma_1\tau} + C$), where Γ_0 and Γ_1 are the characteristic timescales as defined in the main text. Extracted values of Γ_0 and Γ_1 are shown in Fig. 2 c) of the main text and in Fig. 14c) in more detail. The two rates are comparable at these temperatures. Nonetheless, we can identify that one of the rates (Γ_0) remains relatively constant just below a kHz, whereas Γ_1 increases ten-fold between 1.8 and 2.4 K. This is accompanied by a sharp decrease in contrast (that is, in the difference between the transmission signal at $\tau = 10$ μs and at $\tau = 5$ ms).

For these measurements, we fixed the time between P1 and P3 to 26 ms. This provides a minimum value for the recovery time between P2 and P3 of 20 ms, approximately 10 times longer than the longest values of T_1 measured by us. This warrants that any additional spin depletion caused by P2 relaxes before P3 reaches the sample (such that P1 and P3 encounter the sample in the same configuration). We confirm this by analyzing the phase of the signal measured by the lock-in amplifier (Fig. 14 b)) as a function of τ. This phase depends linearly on the delay τ, indicating that any asymmetry between P1 and P3 does not contribute significantly to the measured signal.

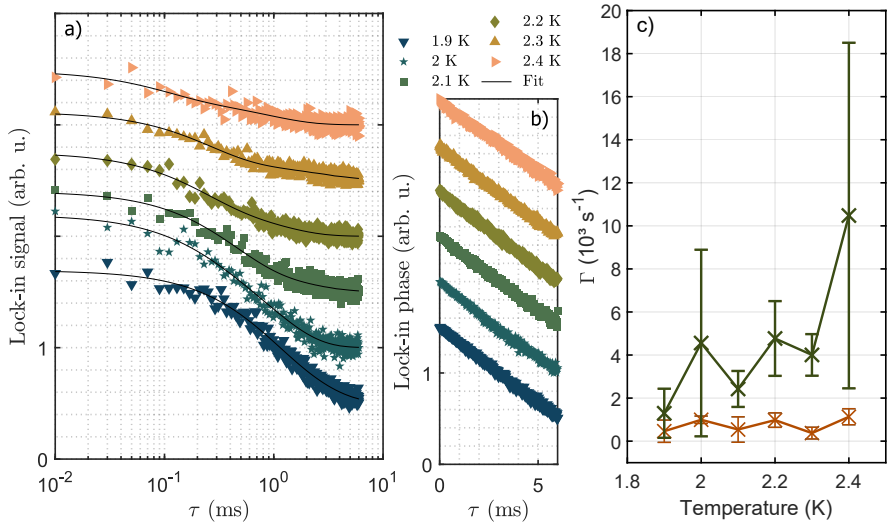

FIG. 14. a) Lock-in signal as a function of the delay τ between P1 and P2 at various temperatures and with a 440 mT magnetic field along the c-axis. We used biexponential fits to the data to functions of the type $y = Ae^{-\Gamma_0\tau} + Be^{-\Gamma_1\tau} + C$ to extract the spin-relaxation rates Γ_0 and Γ_1 between 1.8 and 2.4 K. b) Phase of the lock-in signal. The simple linear dependence between the phase and the delay τ shows that P1 and P3 do not impact the lock-in signal shown in a). c) Relaxation rates extracted from the biexponential fits to the data in a).

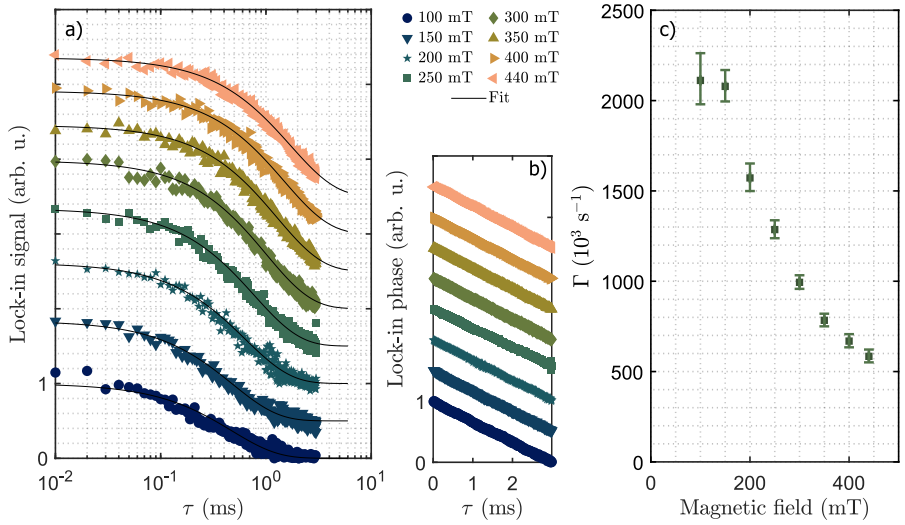

FIG. 15. a) Lock-in signal as a function of the delay τ between P1 and P2 at 2 K and magnetic field along the c-axis between 100 and 440 mT. The short measurement times prevent us from fitting the signals to a biexponential decay function. Instead, we use a fit to a monoexponential decay function ($y = Ae^{-\tau/T_1} + C$) to extract the characteristic timescale T_1 within which most of the relaxation takes place. b) Phase of the lock-in signal. The simple linear dependence between the phase and the delay τ shows that P1 and P3 do not impact the lock-in signal shown in a). c) Rates and respective timescales at which most of the relaxation takes place, showing that spin-relaxation happens 3 times slower at high fields (440 mT) when compared to low fields (100 mT).

E. Magnetic field dependence of T1 at 2 K

Figure 15 a) shows the time-dependent lock-in signal at different amplitudes of the magnetic field applied parallel to the c-axis at 2 K. The traces were normalized with respect to each other and offset vertically for clarity. We extract the spin relaxation time T_1 as a function of magnetic field (Fig. 15 c)) from monoexponential decay fits to the data of Fig. 15 a). For these measurements, we fixed the time between P1 and P3 to 16 ms. Also in this case an analysis of the phase of the signal measured by the lock-in amplifier (Fig. 15 b)) shows that P1 and P3 and do not contribute

significantly to the measured signal.

Figure 15 c) shows a clear magnetic-field dependence of the spin relaxation behavior, with spin relaxation rates that decrease from 2 kHz to 500 Hz as the field increases from 100 to 440 mT. This decrease in the spin relaxation rate is accompanied by an increase in contrast (see also Fig. 2 d) of the main text). Qualitatively this behavior agrees with the existing models for spin relaxation in transition metal defects (see section 10.4 of the textbook Ref. [8], and Ref. [7] for an analysis for the molybdenum defect in 4H-SiC, which is similar to our vanadium defect). In short: when the magnetic field is tuned from the anti-crossing regime (around 50 mT) to higher values, the energy eigenstates of the ground-state spin Hamiltonian become more and more pure Zeeman states. This tuning thus also causes that that the dipole moments for transitions between these levels become smaller. At the same time, the transition energy itself increases with increasing magnetic field (in a relative sense, the environment becomes colder), such that the relevant spectrum of the environment also shifts to higher energies. The exact dependence on magnetic field thereby also depends of the ratio between Zeeman energy and temperature, and on whether the dominant relaxation mechanism is a one-phonon or two-phonon process [7]. All these scenarios give a relaxation rate that at low temperatures shows a strong decrease with increasing magnetic field [8], but more detailed understanding for the vanadium system will require further study.

F. Basics of lock-in detection of an absorption signal in an optical pulse sequence

Since the periodic signal of Fig. 13 is not a very conventional control signal for lock-in detection, we will present here a short derivation of how it is applied. The signal in Fig. 13, with per period the three pulses P1, P2 and P3, represents the modulation of optical power that is incident on the sample. In the sample, part of this optical signal gets absorbed, and after propagating through the sample, this optical signal is detected and leads to a voltage signal $V_S(t)$ from the photodetector. This signal $V_S(t)$ is sketched in Fig. 16b), and it directly reflects the driving with pulses P1, P2 and P3, and we label the three pulses in one period of $V_S(t)$ accordingly. In Fig. 16b), we do not sketch how the top-left form of each pulse is in practice a rounded shoulder, due to the dynamics of optical pumping reaching steady-state populations (for pulses P1 and P3), or due to a relatively small transient from optical-pumping dynamics in the top of P2. This simplification does not compromise the validity of the description below here, and also the quantitative consequences are in our experiments very small and not significant. We ensure that we can treat P2 as a narrow block wave, by having its duration T_{P2} much shorter than the duration of the transients from optical pumping and the ground-state spin relaxation time of the vanadium system. We also ensure that the pulses P1 and P3 in $V_S(t)$ are nominally identical, by making sure that the delays preceding P1 and P3 are well longer than the measured relaxation times (for technical details see Sections V C–V E).

We aim to show here that lock-in detection of $V_S(t)$ (with the lock-in period equal to the period T_{ref} of $V_S(t)$) directly yields a lock-in signal that is proportional to the amplitude (and area) of pulse P2 in the signal $V_S(t)$. For this, we record the lock-in R output (rather than the X or Y quadrature). In our scheme the width of the pulses P2 is constant. Further, in practice, the amplitude of pulse P2 in $V_S(t)$ depends on the P1-P2 delay τ (see Fig. 13), but its pulse shape remains for all τ very similar and close to a narrow block pulse. This means that the amplitude of P2 in $V_S(t)$ (and thus also the lock-in R output) directly reflects how much population is present in the spin levels that are addressed with the laser pulses (see Section V C for further details).

For the analysis, we take as starting point the continuous-time Fourier-series analysis for a simple periodic block wave $V_S(t)$, as in Fig. 16a). The Fourier series representation of this signal is a discrete superposition of complex harmonics with angular frequencies $n \cdot \omega_{ref}$ (with $\omega_{ref} = 2\pi/T_{ref}$), and n running over all the integer numbers. The essence of (first-harmonic) lock-in detection is that it directly measures the amplitude and phase of the component for $n = 1$. For the signal in Fig. 16a) (with pulse duration T_P and pulse amplitude A_P) this $n = 1$ Fourier component is a real number (phase zero), and has the amplitude

$$a_{n=1} = A_P \frac{\sin(\omega_{ref} T_P/2)}{\pi}. \tag{1}$$

The phase zero here means that the first-harmonic detection with the lock-in comes forward as a pure cosine component, if time $t = 0$ is defined in the middle of a pulse of width T_P.

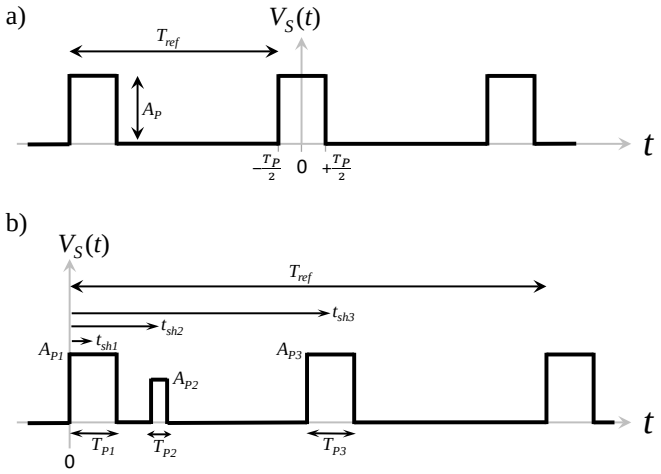

FIG. 16. **a)** A signal $V_S(t)$ that is a periodic block wave, with pulses of height A_P, width T_P, and period T_{ref}. **b)** A signal $V_S(t)$ that is a superposition of three periodic block waves with period T_{ref}. The pulses are labeled as P1, P2 and P3 for their pulse height A_{Pj}, pulse width T_{Pj}, and their time-shift t_{shj} away from having $t = 0$ in the middle of the corresponding block pulse (with $j = 1, 2, 3$).

For using this result for the signal $V_S(t)$ in Fig. 16b), we use the Fourier property that shifting the signal of Fig. 16a) by an amount $+t_{sh}$ to the right, gives in its Fourier series representation each component a phase factor $\exp(-i\omega_{ref}t_{sh})$. If we also use that the signal in Fig. 16b) can be seen as the addition of three periodic block waves, as in

$$V_S(t) = V_{P1}(t) + V_{P2}(t) + V_{P3}(t), \tag{2}$$

the $n = 1$ Fourier component becomes

$$\begin{aligned} a_{n=1} =& A_{P1}\frac{\sin(\omega_{ref}T_{P1}/2)}{\pi} \cdot \exp(-i\omega_{ref}t_{sh1}) + \\ & A_{P2}\frac{\sin(\omega_{ref}T_{P2}/2)}{\pi} \cdot \exp(-i\omega_{ref}t_{sh2}) + \\ & A_{P3}\frac{\sin(\omega_{ref}T_{P3}/2)}{\pi} \cdot \exp(-i\omega_{ref}t_{sh3}), \end{aligned} \tag{3}$$

with symbols T_{P1} and t_{sh1} etc. as defined in Fig. 16b). We experimentally set up conditions where $A_{P1} = A_{P3}$ and $T_{P1} = T_{P3}$, and the timing of pulses P1 and P3 gives $t_{sh3} = t_{sh1} + T_{ref}/2$. This yields that the first and third term in the above equation exactly cancel, and the equation thus simplifies to

$$a_{n=1} = A_{P2}\frac{\sin(\omega_{ref}T_{P2}/2)}{\pi} \cdot \exp(-i\omega_{ref}t_{sh2}). \tag{4}$$

In terms of lock-in detection, this means that the first-harmonic R output is proportional to the amplitude A_{P2} (for any delay τ that we used in our experiments). Since ω_{ref} and T_{P2} are constant during our measurements, and since we have $\omega_{ref}T_{P2}/2 << 1$, this signal is also proportional to the area of P2. In addition, it shows what influence increasing τ should have on the lock-in phase output. As illustrated in Fig. 16b), increasing τ leads to an identical increase of the time-shift t_{sh2}, and this comes forward as a phase shift that behaves as $-\omega_{ref}t_{sh2}$. Such a linear relation between τ and the lock-in phase output is indeed what we observe in our experiments (see Sections V D and V E).

[1] G. Wolfowicz, C. P. Anderson, B. Diler, O. G. Poluektov, F. J. Heremans, and D. D. Awschalom, Vanadium spin qubits as telecom quantum emitters in silicon carbide, Science Advances **6**, eaaz1192 (2020).

[2] P. Cilibrizzi, M. J. Arshad, B. Tissot, N. T. Son, I. G. Ivanov, T. Astner, P. Koller, M. Ghezellou, J. Ul-Hassan, D. White, C. Bekker, G. Burkard, M. Trupke, and C. Bonato, Ultra-narrow inhomogeneous spectral distribution of telecom-wavelength vanadium centres in isotopically-enriched silicon carbide, (2023), arXiv:2305.01757 [quant-ph].
[3] J. Baur, M. Kunzer, and J. Schneider, Transition metals in SiC polytypes, as studied by magnetic resonance techniques, Physica Status Solidi (A) Applied Research **162**, 153 (1997).
[4] R. Kummer, C. Hecht, and A. Winnacker, Persistent spectral-hole burning in the wide-gap semiconductor sic doped with vanadium, Optics Letters **22**, 916 (1997).
[5] C. Hecht, R. Kummer, and A. Winnacker, Persistent spectral-hole burning in sic:v via excited-state absorption, Journal of Luminescence **76-77**, 95 (1998), proceedings of the Eleventh International Conference on Dynamical Processes in Excited States of Solids.
[6] P. Siyushev, H. Pinto, M. Vörös, A. Gali, F. Jelezko, and J. Wrachtrup, Optically controlled switching of the charge state of a single nitrogen-vacancy center in diamond at cryogenic temperatures, Phys. Rev. Lett. **110**, 167402 (2013).
[7] C. M. Gilardoni, T. Bosma, D. van Hien, F. Hendriks, B. Magnusson, A. Ellison, I. G. Ivanov, N. T. Son, and C. H. van der Wal, Spin-relaxation times exceeding seconds for color centers with strong spin–orbit coupling in SiC, New J. Phys. **22**, 103051 (2020).
[8] A. Abragam and B. Bleaney, *Electron paramagnetic resonance of transition ions* (Oxford University Press, 2012).